INTERNATIONAL JOURNAL FOR NUMERICAL METHODS IN FLUIDS
Int. J. Numer. Meth. Fluids 2001; **37**: 175–208 (DOI: 10.1002/fld.173)

A general methodology for investigating flow instabilities in complex geometries: application to natural convection in enclosures

E. Gadoin[a], P. Le Quéré[a,*] and O. Daube[b]

[a] *LIMSI, BP 133, Orsay Cedex, France*
[b] *CEMIF, 40 rue de Pelvoux, CE 1455 Courcouronnes, Evry Cedex, France*

SUMMARY

This paper presents a general methodology for studying instabilities of natural convection flows enclosed in cavities of complex geometry. Different tools have been developed, consisting of time integration of the unsteady equations, steady state solving, and computation of the most unstable eigenmodes of the Jacobian and its adjoint. The methodology is validated in the classical differentially heated cavity, where the steady solution branch is followed for vary large values of the Rayleigh number and most unstable eigenmodes are computed at selected Rayleigh values. Its effectiveness for complex geometries is illustrated on a configuration consisting of a cavity with internal heated partitions. We finally propose to reduce the Navier–Stokes equations to a differential system by expanding the unsteady solution as the sum of the steady state solution and of a linear combination of the leading eigenmodes. The principle of the method is exposed and preliminary results are presented. Copyright © 2001 John Wiley & Sons, Ltd.

KEY WORDS: Arnoldi–Krylov method; flow instabilities; natural convection; Newton's method; numerical algorithms

1. INTRODUCTION

Computation of flow instabilities is certainly one of the most fascinating and challenging aspects of the present computational fluid dynamics. The aim of hydrodynamic instability theory is to predict the values of the parameters at which instabilities occur, the nature of the instability (steady or unsteady, supercritical or subcritical), the type of solution that results from the instability, the modification of the base flow solution that results from the non-linear interactions of the unstable modes and the subsequent route to chaos. Mastering or promoting these instabilities, one aspect of active fluid mechanics, is also a very challenging prospect.

As soon as the geometry involves more than one inhomogeneous spatial direction, one generally lacks analytically known base flow solutions and therefore the stability analysis has

* Correspondence to: LIMSI-CNRS, BP 133, 91403 Orsay Cedex, France.

Received 15 October 1999
Revised 9 August 2000

to be carried out numerically by resolution of the governing equations. This is usually done by direct integration of the unsteady Navier–Stokes equations. This methodology places severe constraints on the numerical algorithms, which must be both spatially and time accurate. This has in particular promoted the development of spectral and pseudo-spectral spatial Chebyshev approximations in space coupled to second-order time stepping schemes. It is indeed true that these unsteady methods have proven extremely successful in predicting loss of stability of several classes of flows, although like any other method, they have to be used with sufficient grid resolution. While these methods are still heavily used in this context and also to perform direct numerical simulations of flows in simple geometries, they have also shown their limitations in establishing bifurcation diagrams and for complex geometries.

For the purpose of investigating the stability of flows in general, it has been recognized [1] that it is highly desirable to have efficient solvers to follow the path of steady solution branches even when they become unstable. Designing a solver to compute the unstable steady solutions is not a trivial matter since it is almost mandatory to use Newton's iterations, coupled in general to arc length continuation. Newton's iterative technique makes use of the Jacobian of the equations, which is on the order of three to four times the number of discretization points in two spatial dimensions. When the instability takes place at large values of the Reynolds or Rayleigh number, as is the case for flows between rotating disks or for natural convection in differentially heated cavities, the number of discretization points needed to approximate the solution can become very large. Building the corresponding Jacobian matrix may also become difficult, in particular in the context of finite volume staggered meshes,[1] although it is very sparse. Furthermore, the incompressibility constraint in velocity–pressure formulation makes this matrix not easily invertible. Matrix free methods are therefore needed, i.e. a method which requires only the evaluation of the action of the Jacobian on a vector field to produce a solenoidal vector field, but this is not an easy task either due to the bad conditioning of the matrix.

An elegant solution to this problem was proposed by Tuckerman [2,3] based on the fact that a family of efficient time stepping algorithms have been developed for integrating the unsteady equations. These are generally based on an implicit treatment of the viscous terms and an explicit treatment of the non-linear terms. She noted that the operator consisting of the difference between the solutions at two consecutive time steps has the same roots as the steady state operator; a simple but far-reaching observation indeed, since it turns out that the Jacobian of the incremental operator is a straightforward modification of the initial time stepping scheme and can thus be used very efficiently in the Newton's iterations. To date, most implementations have been performed for simple geometries in which the unsteady Stokes problem is solved by direct algorithms such as implicit influence matrix methods either with finite differences or spectral methods [4]. Our experience with this algorithm has shown us that a key point in the efficiency and global performance of the method seems related to the fact that the time stepping solver simultaneously enforces the discrete momentum and continuity equations (Dr LS Tuckerman, private communication) although there have been successful

[1] This objection does not hold for the finite element community, which has usually employed the true Newton's method, as it did not benefit from the natural separability of the operators, even on structured meshes.

implementations with fractional step algorithms [5,6]. One of our objectives in this work is to propose an extension of the method applicable to convection dominated flows in moderately complex geometries such as, for example, natural convection in cavities with internal partitions. To this aim we have implemented an iterative solver of the unsteady Stokes problem discretized on a classical staggered grid based on Vanka's multigrid scheme [7].

Once a steady solution is obtained, its linear stability can be investigated in several ways. One possibility is to perform time integration of the linearized equations governing the fluctuations. This is most efficiently done by adapting an unsteady code such as a fractional step method for the integration of the equations governing the fluctuating quantities with the quadratic non-linearities and replaced by linearized quantities about the steady solution. Integrating these unsteady equations will then eventually 'polarize' the fluctuating solution along the most unstable (or least stable) eigenmode. This method works generally well if the few most unstable eigenmodes are sufficiently far apart although it is necessary to use small enough time steps so that it may require integrating over several tens or hundreds of thousands of time steps in order for the solution to polarize. It can also be highly non-monotonic in the sense that, even if the base flow solution is stable, the energy of the fluctuations can grow substantially before reaching its asymptotical decaying rate. The amplitude of this energy growth is related to the non-normality of the Jacobian [8], which increases as the relative size of the viscous terms to the convective terms decreases.

Another technique is to compute the spectrum of the Jacobian which gives access to the Jacobian eigenvalues. The solution will be linearly stable if all eigenvalues are of negative real part, unstable otherwise. Some implementations of this methodology have been based on an explicit representation of the Jacobian and on the use of generalized eigensolvers such as QR algorithms [9]. This approach seems limited to configurations which undergo instability at small Reynolds or Rayleigh number values, thus amenable to small or moderate spatial resolutions. When this is not the case, the memory requirements for storing the Jacobian can become prohibitively large. Further, it is even useless to compute the whole spectrum since it is only those eigenvalues of the Jacobian of the largest real part, which are of interest. These two remarks have led to the development of Arnoldi–Krylov algorithms, which allow for the computation of a selected part of the spectrum using matrix free methods. An invariant low dimensional subspace is determined by the repeated action of the Jacobian operator on an initial iterate; the corresponding eigenmodes are then computed in this space. This was done in this work by using the ARPACK library [10].

Our last objective is to establish a methodology to reduce the dynamics of the corresponding flows to a low dimensional dynamical system. We propose to expand the unsteady solution in a basis consisting of some of the most unstable eigenmodes. After substitution of this expansion in the governing equations, obtaining the dynamical system requires taking the inner product with the orthogonal functions, which are the eigenmodes of the adjoint of the Jacobian. It is also well known that these adjoint eigenmodes are instrumental for the purpose of controlling the flow [11].

This paper is organized as follows: we will present in the next section the equations that govern the flows and configurations in which we are interested. The following three sections will be devoted to the description of the numerical algorithms needed throughout this work.

First, the main features of the unsteady algorithm that underlie the whole work will be reminded.

Then, the computation of branches of steady solutions will be addressed and its efficiency will be illustrated by computing the solutions on the steady branch for the differentially heated cavity of aspect ratio 4 for values of the Rayleigh number more than one order of magnitude above the critical value and for a cavity with internal heated partitions representative of cooling of electronic equipment. The following section will address the determination of the spectrum of the Jacobian of the Navier–Stokes equations linearized about the solutions on the steady branch. Illustrative examples will be given for the corresponding configurations.

Lastly, we will address the determination of the adjoint Jacobian spectrum and the principle of generating the dynamical system will be discussed.

2. GOVERNING EQUATIONS

The class of flows in which we are interested are modelled with the Navier–Stokes equations in the Boussinesq approximation. The fluid is characterized by constant kinematic and thermal diffusivities ν and κ respectively, assumed to be constant. It is enclosed in a two-dimensional cavity of height H and width ℓ, corresponding to a vertical ratio aspect $R_F = H/\ell$. The corresponding equations are made dimensionless by introducing $L_{\mathrm{ref}} = H$, $V_{\mathrm{ref}} = (\kappa/H)Ra^{1/2}$ and $t_{\mathrm{ref}} = (H^2/\kappa)Ra^{-1/2}$ as reference quantities for length, velocity and time, where Ra is the Rayleigh number based on H $(= g\beta H^3 \Delta T/\nu\kappa)$ and Pr $(= \nu/\kappa)$ is the fluid Prandtl number. The dimensionless temperature is defined as $\Theta = (T - T_1)/(T_2 - T_1)$, where T_2 and T_1 are the hot and cold temperatures applied at cavity walls. The governing equations can then be cast in the following non-dimensional form:

$$\frac{\partial u}{\partial x} + \frac{\partial w}{\partial z} = 0 \tag{1}$$

$$\frac{\partial u}{\partial t} + u\frac{\partial u}{\partial x} + w\frac{\partial u}{\partial z} = -\frac{\partial P}{\partial x} + \frac{Pr}{\sqrt{Ra}}\nabla^2 u \tag{2}$$

$$\frac{\partial w}{\partial t} + u\frac{\partial w}{\partial x} + w\frac{\partial w}{\partial z} = -\frac{\partial P}{\partial z} + \frac{Pr}{\sqrt{Ra}}\nabla^2 w + Pr\Theta \tag{3}$$

$$\frac{\partial \Theta}{\partial t} + u\frac{\partial \Theta}{\partial x} + w\frac{\partial \Theta}{\partial z} = \frac{1}{\sqrt{Ra}}\nabla^2 \Theta \tag{4}$$

where t is the time, u and w are the velocity components in the x (horizontal) and z directions respectively and P the dimensionless deviation from the hydrostatic pressure. In these equations, ∇^2 is the laplacian operator $(\partial^2/\partial x^2 + \partial^2/\partial z^2)$.

We have considered two geometrical configurations. The first one is the classical differentially heated cavity (Figure 1). The left wall is maintained at the hot temperature, the right one at the cold temperature whereas the walls at top and bottom are adiabatic. We will consider

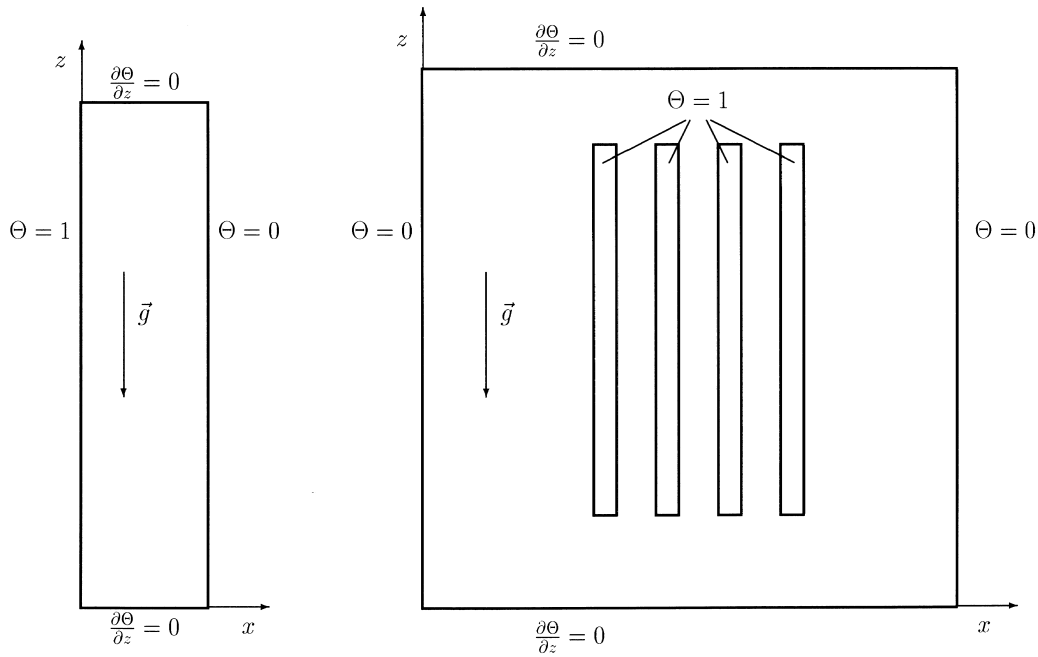

Figure 1. Problem geometry and temperature boundary conditions for differentially heated cavity (left) and partitioned cavity (right).

a cavity of aspect ratio $H/\ell = 4$, which was investigated in detail in the past [12]. This will help demonstrate the efficiency of the methods described hereafter. The second geometrical configuration is representative of problems met in passive cooling of electronic equipment. It consists of a square cavity with four internal heated vertical plates featuring electronic boards (Figure 1). The internal plates are heated while the outer vertical walls are cold, the top and bottom walls being adiabatic. This will help illustrate the capability of the methodology for (relatively) complex geometries.

3. NUMERICAL ALGORITHMS

As said in Section 1, investigating the stability of the solutions of the Navier–Stokes equations require the joint use of several algorithms either capable of integrating the unsteady equations or of solving the steady state equations. Although the main emphasis of this paper is on the steady state solver and the subsequent determination of the Jacobian spectrum, we first begin by recalling briefly, for the sake of completeness, the basic unsteady time stepping scheme used to integrate the unsteady Equations (1)–(4).

3.1. Unsteady solving

For the stability problem of interest, first-order time stepping is not adequate since, from experience, the amplitude of the fluctuations depends strongly on the time step and the use of a higher-order time stepping scheme is mandatory. We use a second-order scheme fractional step method, which is based upon two main ingredients [13]:

– the time derivative in the momentum and in the energy equations is approximated by a second-order backward differentiation formula

$$\frac{\partial f^{n+1}}{\partial t} = \frac{3f^{n+1} - 4f^n + f^{n-1}}{2\Delta t} + \mathcal{O}(\Delta t^2)$$

– the linear terms L are implicitly evaluated at time $(n+1)\Delta t$, whereas the non-linear part NL is explicitly evaluated at time $(n+1)\Delta t$ by means of a linear extrapolation

$$NL^{n+1} = 2NL^n - NL^{n-1}$$

This time stepping scheme yields a Helmholtz-type problem for $(u^{n+1}, v^{n+1}, p^{n+1}, \Theta^{n+1})$ in which the energy equation (4) is decoupled from the momentum (2)–(3) and continuity (1) equations

$$(\sigma_\theta I - \nabla^2)\Theta^{n+1} = S_\theta^{n,n-1}$$

$$(\sigma_v I - \nabla^2)\mathbf{V}^{n+1} + \nabla p^{n+1} = \mathbf{S}_v^{n,n-1}$$

$$\nabla \cdot \mathbf{V}^{n+1} = 0$$

where $\sigma_\theta = 3\sqrt{Ra}/2\Delta t$ and $\sigma_v = \sigma_\theta / Pr$. The source terms $S_\theta^{n,n-1}$ and $\mathbf{S}_v^{n,n-1}$ contain all the quantities which are evaluated at the previous time steps.

The velocity–pressure coupling is handled by using an incremental projection method [14] which classically consists in two steps:

– a prediction step in which a provisional velocity field $\mathbf{V}^*$ is computed

$$(\sigma I - \nabla^2)\mathbf{V}^* = -\nabla p^n + \mathbf{S}^{n,n-1} \tag{5}$$

$$\mathbf{V}^* = 0 \quad \text{on } \Gamma \tag{6}$$

– a projection step in which $\mathbf{V}^*$ is expressed, using the Helmholtz decomposition theorem, as the sum of its divergence free part, which is called $\mathbf{V}^{n+1}$, and of its irrotational part, which can be written $\nabla\psi$, i.e.

$$\mathbf{V}^* = \mathbf{V}^{n+1} + \nabla\psi \tag{7}$$

$$\nabla \cdot \mathbf{V}^{n+1} = 0 \tag{8}$$

$$\mathbf{V}^{n+1} \cdot \mathbf{n} = 0 \quad \text{on } \Gamma \tag{9}$$

The prediction step thus yields two Helmholtz equations that can be solved independently. Each one of the three Helmholtz equations for temperature or both velocity components gives rise, after space discretization, to a linear system of equations which can be solved using iterative matrix free methods such as GMRES [15]. An alternate way is to solve these linear systems by means of a non-iterative classical Peaceman–Racheford alternating direct implicit (ADI) scheme, in which second-order time accuracy is retained if one reformulates the Helmholtz equation (5) in an Helmholtz equation for the increment between two consecutive time steps.

The projection step can be recast, setting $\psi = \frac{2}{3}\Delta t\phi$, as

$$\mathbf{V}^{n+1} = \mathbf{V}^* - \frac{2}{3}\Delta t\nabla\phi \tag{10}$$

$$\nabla \cdot \mathbf{V}^{n+1} = 0 \tag{11}$$

$$\mathbf{V}^{n+1} \cdot \mathbf{n} = 0 \quad \text{on } \Gamma \tag{12}$$

This projection is actually performed by taking the divergence of (10), which yields a Poisson-type equation for ϕ, which reads

$$\nabla \cdot \nabla\phi = \frac{3}{2\Delta t}\nabla \cdot \mathbf{V}^* \tag{13}$$

$$\nabla\phi \cdot \mathbf{n} = 0 \quad \text{on } \Gamma \tag{14}$$

This equation is solved most efficiently by a multigrid technique. Note that the use of classical staggered grid discretization results in the fact that the corresponding discrete problem has a kernel of dimension 1 and that the imposed boundary condition (6) ensures that the associated compatibility condition is automatically satisfied. The computation of ϕ allows for the determination of $\mathbf{V}^{n+1}$ and p^{n+1} according to

$$\mathbf{V}^{n+1} = \mathbf{V}^* - \frac{2}{3}\Delta t\nabla\phi \tag{15}$$

$$p^{n+1} = p^n + \phi \tag{16}$$

One should note that the use of these ingredients (incremental projection method and incremental ADI formulation or GMRES solving for the uncoupled Helmholtz equations), allows one to get the *exact* discrete solution of the coupled energy, momentum and continuity equations if the solution reaches a steady state.

This time stepping scheme can be trivially modified, once a steady state solution U_0 has been obtained (which is the subject of the next section), to integrate the Navier–Stokes equations expressing the unsteady solution as $U_0 + \tilde{U}$, where $\tilde{U}$ is the fluctuating part of the solution. Note that this decomposition allows for the integration of full non-linear or of the linearized equations, thus allowing one to determine the nature (sub- or supercritical) of the first bifurcation.

3.2. Steady state solving

3.2.1. Algorithm description. The steady state solutions of Equations (1)–(4) satisfy

$$\frac{\partial u}{\partial x} + \frac{\partial w}{\partial z} = 0 \tag{17}$$

$$u\frac{\partial u}{\partial x} + w\frac{\partial u}{\partial z} = -\frac{\partial P}{\partial x} + \frac{Pr}{Ra^{1/2}}\nabla^2 u \tag{18}$$

$$u\frac{\partial w}{\partial x} + w\frac{\partial w}{\partial z} = -\frac{\partial P}{\partial z} + \frac{Pr}{Ra^{1/2}}\nabla^2 w + Pr\Theta \tag{19}$$

$$u\frac{\partial \Theta}{\partial x} + w\frac{\partial \Theta}{\partial z} = \frac{1}{Ra^{1/2}}\nabla^2 \Theta \tag{20}$$

Let us call $U_0 = (\bar{u}, \bar{w}, \bar{P}, \bar{\Theta})$ such a steady state. In shorthand notation, U_0 satisfies

$$(L - N(U_0)) \cdot U_0 = 0 \tag{21}$$

with the constraint that the velocity field $(\bar{u}, \bar{w})$ be divergence free. Solving these equations directly is not easy even when the corresponding solution is stable. Because they are non-linear, iterative techniques must be used. Several algorithms have been developed for this purpose although the convergence of most of them degrades as the Rayleigh number increases, i.e. when the equations become increasingly convection-dominated. Solving for an unstable steady state solution is far more difficult because iterative techniques based on pointwise relaxation generally fail to converge when the relaxation operator is not definite, and Newton's methods, long used in the finite element community but no so much in the context of finite differences or finite volumes discretizations, seem preferable. Starting from an initial guess U^0, one Newton step consists of computing an increment $\Delta U^k = U^{k+1} - U^k$ which is the solution of

$$(L - DN_{U^k}) \cdot \Delta U^k = -(L - N(U^k)) \cdot U^k \tag{22}$$

where $((L - DN_{U^k}) = \mathscr{L}_{U^k})$ is the Jacobian of the non-linear operator about the current iterate U^k. It is again understood that the velocity components of the increment must be divergence-free. It is well known that this method converges quadratically once U^k gets sufficiently close to U_0.

While this procedure is simple in principle, its application to the incompressible equation raises many difficulties. The first one is due to the size of the Jacobian, typically $4 \times NI \times NJ$ (where NI and NJ are the number of grid points in each spatial direction) when dealing with the two velocity components, pressure and temperature. The order of the Jacobian can thus become prohibitively large for problems in which the instability occurs at large values of the Rayleigh number and which therefore need fine mesh sizes to be adequately resolved. Second, it is often difficult to provide an explicit matrix representation of the Jacobian. Lastly, even if this Jacobian is made available, its inversion it virtually impossible due to its poor conditioning.

While the direct inversion of the full steady non-linear (21) or linearized (22) equations is almost impossible, it turns out that efficient schemes have been derived to solve the unsteady Stokes problem. This operator stems from the time discretization of the unsteady non-linear equations (1)–(4) using an implicit time stepping scheme for the viscous diffusion terms coupled to an explicit treatment of the non-linear terms. Such a first-order scheme can be written as

$$\frac{U^{n+1} - U^n}{\delta t} = L \cdot U^{n+1} - N(U^n) \cdot U^n \tag{23}$$

where it is again understood that the velocity field which is part of U^{n+1} be divergence free. Equation (23) can be cast into the following form:

$$(I - \delta t L) U^{n+1} = (I - \delta t N(U^n)) U^n \tag{24}$$

Efficient schemes have been developed to integrate these equations either for the velocity–pressure formulation or for the two-dimensional stream function–vorticity formulation. They are generally based either on the direct inversion of the Uzawa algorithm or on so-called influence matrix techniques that make use of the linear relationships between the pressure and the divergence of the velocity field at the boundary of the computational domain in the velocity–pressure formulation or between the vorticity and normal derivative of the stream function at the boundary in the stream function–vorticity formulation [16–19]. These algorithms are generally restricted to simple geometries, as the building of the influence matrix can become complex for irregular geometries, in addition to the fact that most of these methods use direct methods for the inversion of the Helmholtz-type equations. Due to the explicit treatment of the non-linear terms these methods suffer from conditional time step stability criteria, which may require integrating for a large number of time steps, in particular when approaching bifurcation points.

Tuckerman [2,3] showed how to make use of such algorithms to compute quite easily the steady state solution. Let us call $E_{\delta t} U^n = (U^{n+1} - U^n)/\delta t$, where n and $n+1$ represent two consecutive time steps. From Equation (24), one has

$$E_{\delta t}U^n = \frac{(I-\delta tL)^{-1}(I-\delta tN(U^n))-I}{\delta t}\,U^n \tag{25}$$

$$= (I-\delta tL)^{-1}(L-N(U^n))U^n \tag{26}$$

and $E_{\delta t}U=0$ has as roots the steady solutions of Equation (21), since $(I-\delta tL)^{-1}$ is non-singular. Applying Newton's method to $E_{\delta t}U=0$ is equivalent to determining increments ΔU^k to the current iterate U^k that are solutions of the linear system

$$DE_{\delta t}\Delta U^k = -E_{\delta t}U^k \tag{27}$$

where $DE_{\delta t}$ is the Jacobian of $E_{\delta t}$ evaluated on U^k. It is easy to see that

$$DE_{\delta t} = (I-\delta tL)^{-1}(L-DN_{U^k}) \tag{28}$$

$$= \frac{(1-\delta tL)^{-1}(I-\delta tDN_{U^k})-I}{\delta t} \tag{29}$$

where DN_{U^k} is the Jacobian of N evaluated on U^k. Starting with an initial guess U^0, for each Newton iteration, the right-hand side of Equation (27) is computed by integrating over one time step the unsteady non-linear equations and evaluating the increment from U^n to U^{n+1}. The increment ΔU^k can then be computed using matrix the free methods (we have used GMRES [15]) which only require computing the action of the operator $DE_{\delta t}$ on a given vector. One such evaluation is equivalent to integrating over one time step the unsteady Stokes problem.

Note that the time step δt acts as a convergence parameter and should be chosen in order to improve convergence of the global iterative scheme. Numerous experiments have shown that δt should be taken very large (10^4 or larger). In this case the unsteady term in the unsteady Stokes operator becomes negligible and one essentially deals with the Stokes operator, which is strongly elliptic. This remark turns out to be essential when solving the Stokes operator with iterative methods, which are needed if one wants to address relatively complex geometries.

3.2.2. Spatial discretization. We have chosen to discretize the equations using the classical staggered grid arrangement in which the computational domain is covered with grid cells. The scalar variables, pressure and temperature, are defined at cell centres, whereas the velocity components are defined at the cell boundaries. If the domain is covered with $NI \times NJ$ cells in the x- and z-direction respectively, the total number of unknowns is thus $(NI+1)NJ + NI(NJ+1) + 2 \times NI \times NJ$. The diffusive and convective fluxes are discretized with centred differences.

3.2.3. Solution of the unsteady Stokes problem. As already said, a very efficient Stokes solver is needed, since it is called on many times. Previous implementations have generally made use of direct Stokes solvers [4]. For complex geometries, iterative Stokes solvers are more flexible and seem therefore preferable. A further requirement is that this solver remain efficient for high spatial resolutions, since the problems we want to address are characterized by thin wall

boundary layers that require good spatial resolutions as the Rayleigh number increases. Amongst all iterative methods, multigrid methods are known to achieve an efficiency that does not deteriorate as the spatial resolution increases [34,35]. They work best for strongly elliptic operators and, in view of the remark made above, they therefore seem to be ideally suited for our purpose.

We have thus implemented the multigrid procedure proposed by Vanka [7]. On a given grid the local smoother consists of solving for each cell the linear system of order 5 made of four momentum equations (two in each direction) coupled to the continuity equation. Whereas we have been somewhat unsuccessful in the past in applying this method to the full non-linear equations at large Rayleigh number, its application here is much more straightforward. Since we are dealing with a linear problem, a straightforward correction scheme can be used instead of the full multigrid algorithm FMG FAS used in the non-linear case, where the current solution must be defined on the coarse grids. We have chosen to define the linear operators directly on the coarse grids as the natural discretization of the operators on the corresponding grids. The restriction of the residuals of the momentum and continuity equations is defined as the weighted sums of the residuals. The extension of the corrections is defined as bilinear interpolations.

3.2.4. Adaptations for complex geometries. This algorithm is made to work for 'complex' geometries by defining a phase indicator, defined at the same location as the scalar variables, which takes value 1 for a fluid cell and 0 for a solid cell. This phase indicator is defined on the fine grid and its values on the coarser grids are defined recursively in the following manner. Since a coarse cell corresponds to the clustering of four fine cells, it is assumed to be a solid cell iff all four fine cells are solid, otherwise it is considered a fluid cell. With the help of this phase indicator all the operators and their boundary conditions can be defined automatically on all grids.

4. NUMERICAL VALIDATION

4.1. Differentially heated cavity

As a test, the natural convection flow in a differentially heated cavity of aspect ratio 4 is computed. In such a cavity with adiabatic top and bottom walls, the steady solution looses its stability at a Rayleigh number Ra just above 10^8. (The critical width based Rayleigh number is $Ra_W = 1.61 \times 10^6$, see [12].)

The implementation of Newton's method is first validated by computing the steady solution for $Ra = 6.4 \times 10^7$, that is a Rayleigh number value less than the critical value. This required eight Newton's iterations to decrease the residuals of the temperature, momentum and continuity equations to machine accuracy, and the total number of Stokes solves was less than 1000. Each Stokes solve required approximately 15 multigrid V-cycles. The corresponding solution is compared with the steady state solution of the non-linear problem obtained with the time integration scheme described in Section 3. Figure 2 displays the time evolution of the L_2 norm of the difference between the transient solution and the steady Newton solution for $Ra = 6.4 \times 10^7$. The initial condition for the time integration was the steady solution for

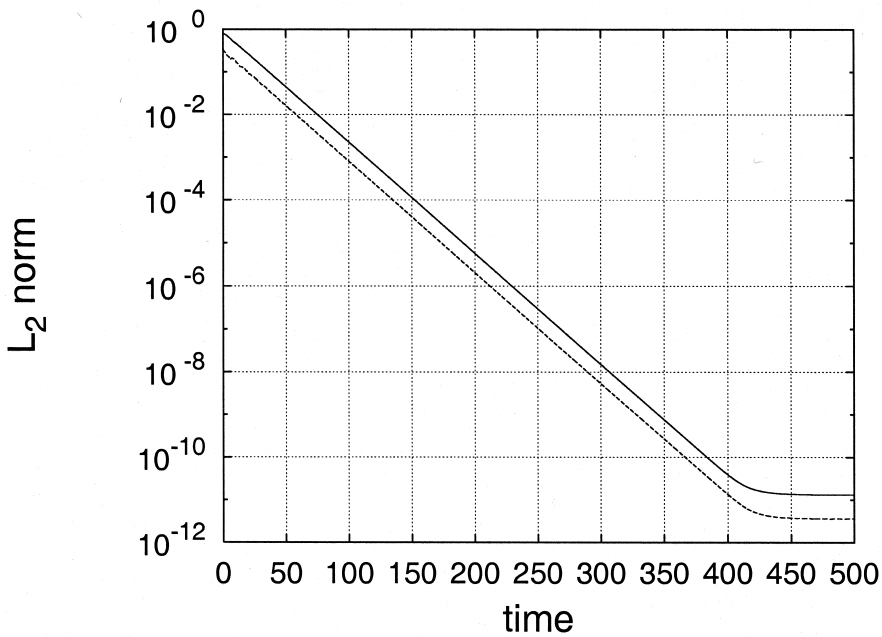

Figure 2. Temporal evolution of the L_2 norm of the difference between the unsteady solution and the steady Newton solution: $\sqrt{\Sigma_{i,j}(\theta_{ij}(t) - \theta_{ij}(\text{Newton}))^2}$ at $Ra = 6.4 \times 10^7$ for differentially heated cavity. Temperature, full line; vertical velocity, dotted line.

$Ra = 6.4 \times 10^6$. It indeed shows that, as time goes to infinity, the L_2 norm of the difference decreases to machine accuracy, confirming that both procedures allow us to obtain exactly the same discrete solution of the coupled equations. It should also be noted that reaching the steady state with the time integration scheme to within machine accuracy required more than 100 000 time steps, as the time step was limited for stability constraints to 0.004 (this number would obviously increase as the Rayleigh number would approach the critical value). This should be compared with the number of Stokes solves, although the amount of work for one multigrid Stokes solve is much larger than that needed to advance one time step in the prediction–projection algorithm. Although a direct comparison of CPU times is not meaningful,[2] a clear advantage of Newton's method is that machine accuracy can be obtained in a few iterations once the region of quadratic convergence is reached.

As a proof of the effectiveness of the method, the unstable steady solution is computed for values of the Rayleigh number larger than the critical value up to 2.02×10^9 ($Ra_W = 10^{7.5}$). The mesh is uniform and kept fixed to 64×128 up to $Ra = 10^8$ and increased to 128×256 for

[2] The time stepping scheme runs on a vector machine like a Cray-C90 at a speed of about 400 Mflops. The multigrid Stokes solver performs very poorly on this type of machine and the code was thus run on an SGI O2K.

larger values. This proved to be enough up to 10^9 at which there are still seven points in the thermal boundary layer. Table I gives numerical details for conditions of the simulations. The pseudo-time step δt is set to 10^5. In most cases, convergence was obtained in less than 20 Newton steps starting from the preceding Rayleigh number solution (Table I). The efficiency of convergence, shown in Figure 3, allows one to reduce the norm of the right hand side of Equation (27) of about a factor ten for each Newton step. Quadratic convergence was not always obtained because within each Newton step the total number of GMRES iterations was kept less than a preset number (usually on the order of 100 or so), precluding computation of the exact increment. The total number of Stokes solves to compute each solution was thus less than 2000, which can be considered as small compared with the number of time steps. It should also be said that, as expected, convergence of the method becomes slower as the Rayleigh number is increased. The major difficulty we have encountered is that the restarted GMRES algorithm sometimes failed to converge. The residual did not decrease over the prescribed maximum number of iterations and the norm of the right-hand side of Equation (27) could not be decreased to machine accuracy. We have tried other solves, such as biconjugate gradient squared, which did not solve the difficulty. One remedy was to decrease

Table I. Computed steady solutions and corresponding spatial discretization.

Ra	6.4×10^6	6.4×10^7	1.28×10^8	1.6×10^8	1.6×10^8	1.92×10^8	6.4×10^8	2.02×10^9
Mesh	64×128	64×128	64×128	64×128	128×256	128×256	128×256	128×256
Step	5	8	8	8	10	11	13	20

Last line gives the number of Newton steps starting from the solution obtained for the immediately smaller Rayleigh number as an initial guess.

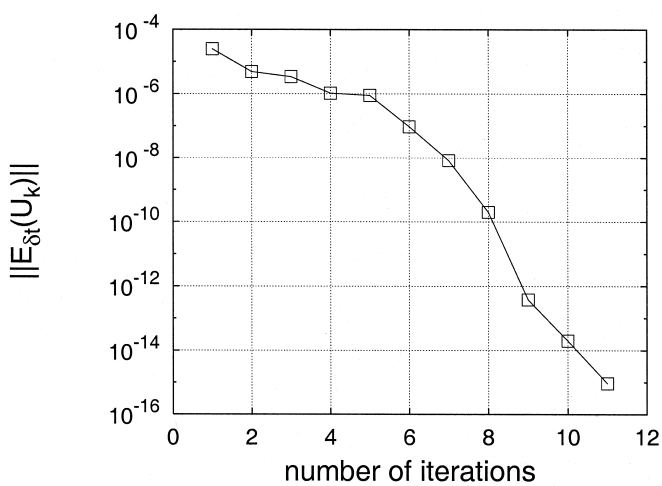

Figure 3. Convergence of Newton's method for differentially heated cavity at $Ra = 1.92 \times 10^8$.

the Rayleigh number increment (since we did not use any continuation of the steady solution branch at $Ra = 2.02 \times 10^9$ ($\simeq 20$ times the critical value). Solving these difficulties is the subject of current research.

Figure 4 shows the temperature fields for each solution. All these solutions share the usual common flow features: two thin boundary layers along the vertical walls and a vertically stratified core region. The thermal stratification $\partial\Theta/\partial z$ is almost uniform throughout the cavity core, and except for the first value of the Rayleigh number, it becomes constant and very close to 1 in units of $\Delta T/H$ at mid-height as shown in Figure 5. Temperature and vertical velocity profiles across the boundary layer at mid-height are displayed in Figure 6. The thickness of the thermal and the dynamic boundary layers decrease as the Rayleigh number increases, whereas the maximum vertical velocity remains almost constant and equal to 0.22. When the distance to the wall is scaled by $Ra^{1/4}$, all profiles collapse onto a single curve, which indicates that the laminar boundary layer scalings [20,21] remain asymptotically valid. Likewise, the corresponding Nusselt number (Table II) continues to scale like $Ra^{1/4}$ with a proportionality constant very close to 0.313. This sequence of unstable solutions on the steady solution branch has thus helped us to establish the asymptotic structure of the steady laminar separated boundary layer regime, in particular concerning the boundary layer thickness and the vertical stratification in the core.

4.2. Cavity with internal plates

This configuration was selected both because of its relevance to cooling of electronic equipment and as a test of the efficiency of the algorithm for moderately complex geometries. This

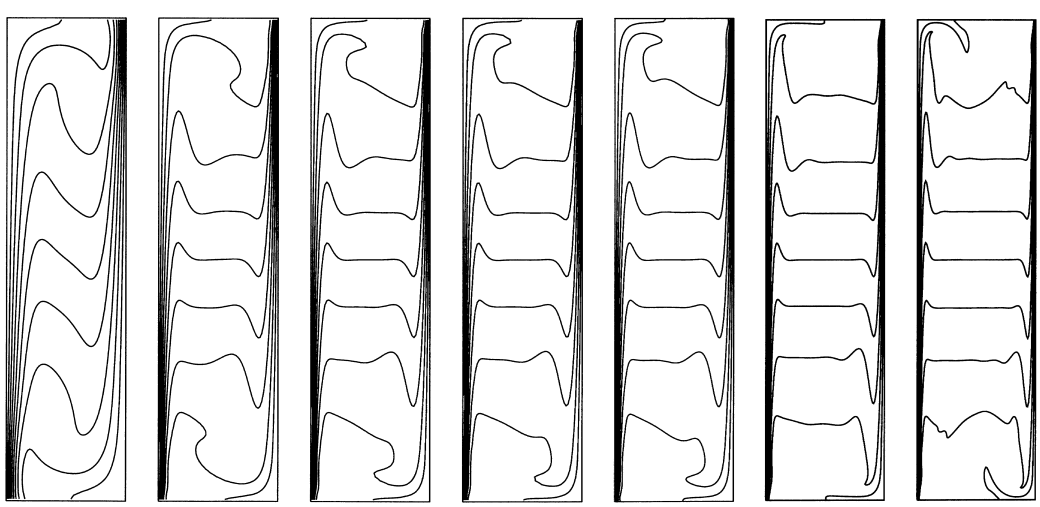

Figure 4. Temperature field for steady states for differentially heated cavity, from left to right: $Ra = 6.4 \times 10^6$, $Ra = 6.4 \times 10^7$, $Ra = 1.28 \times 10^8$, $Ra = 1.6 \times 10^8$, $Ra = 1.92 \times 10^8$, $Ra = 6.4 \times 10^8$, $Ra = 2.02 \times 10^9$ (isovalues are: 0.1, 0.2, 0.3, 0.4, 0.5, 0.6, 0.7, 0.8, 0.9).

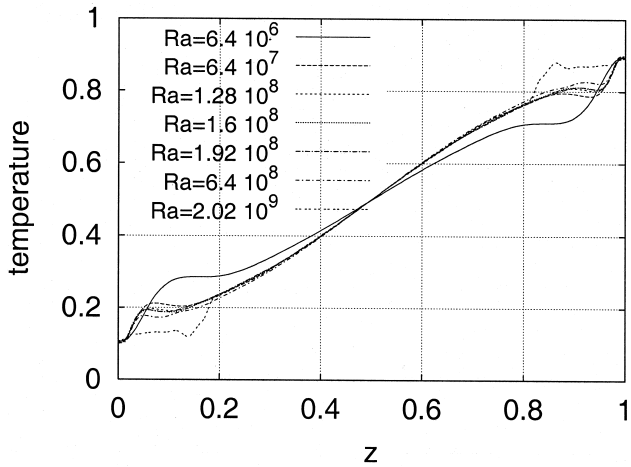

Figure 5. Temperature profiles at mid-width for steady states for differentially heated cavity.

geometry is appropriately described through the use of the phase indicator because the solid area is small compared to the fluid area. For this configuration, the value of critical Rayleigh number is slightly above 10^8 [22].

As for the differentially heated cavity, the implementation of Newton's method is first validated by comparing the steady solution for a Rayleigh number of $Ra = 1.0 \times 10^7$, less than the critical value, with the asymptotic solution of the non-linear problem with the time integration scheme. The comparison between both solutions shows a perfect agreement as the L_∞ norm of the difference is smaller than 10^{-10}. Reaching the steady state with the unsteady integration to that level of accuracy required integrating the equations for a total time of 500 with a time step of $\delta t = 0.01$, that is approximately 5×10^4 time steps.

Computations were performed with a 128×128 uniform mesh for Rayleigh number values up to $Ra = 1.0 \times 10^7$ and with a 256×256 uniform mesh for $Ra = 1.0 \times 10^8$. For $Ra = 1.0 \times 10^8$, 15 Newton steps were necessary to obtain the steady state starting from the solution at $Ra = 1.0 \times 10^7$ (Figure 7). For each Newton step, the number of GMRES iterations was limited to 80 and the 15 Newton's iterations thus required 1200 solutions of the Stokes problem, which is again much smaller that the number of time steps. Each Stokes solution was obtained in about 20 multigrid V-cycles.

Figure 8 shows the temperature and velocity fields of the solution at $Ra = 1.0 \times 10^8$. The flow goes up along the vertical plates, crosses the cavity at the top and then flows down along the cold walls into two thin boundary layers, which rebound against the adiabatic floor to feed the vertical channels and the vertical boundary layers along the outer heated walls. Concerning the temperature field, it can be seen that the upper part of the cavity is almost isothermal at the hot temperature, and that the vertical stratification is limited to

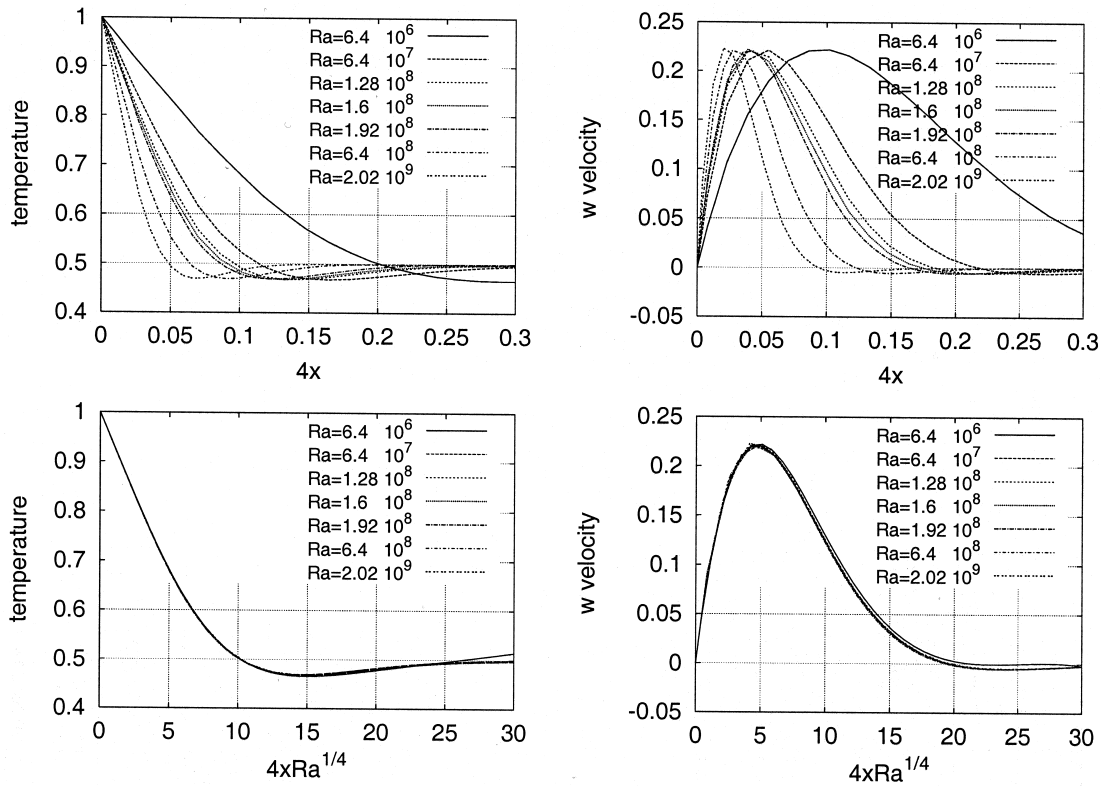

Figure 6. Temperature and vertical velocity profiles at mid-height for steady states for differentially heated cavity.

Table II. Nusselt number and correlation.

Ra	6.4×10^6	6.4×10^7	1.28×10^8	1.6×10^8	1.92×10^8	6.4×10^8	2.02×10^9
Nu	15.56	27.87	33.37	35.37	36.83	49.53	67.30
$Nu/Ra^{1/4}$	0.309	0.312	0.314	0.314	0.313	0.311	0.317

the lower two thirds of the outer core regions, where it reaches locally values as high as 1.3. Horizontal temperature profiles show that, in the lower part of the cavity, the temperature is slightly lower inside the chimneys than in the core region, which is the distinctive mark of the chimney effect.

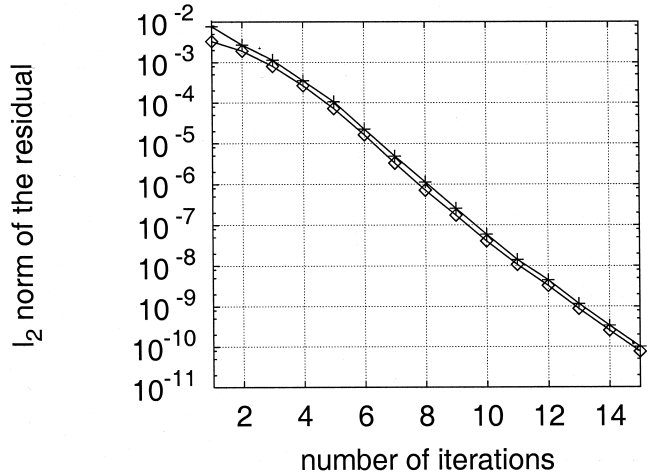

Figure 7. Convergence of Newton's method for partitioned cavity at $Ra = 1.0 \times 10^8$; evolution of norm of residuals of Equation (21) for: u-velocity, ($\diamond$); w-velocity, ($+$).

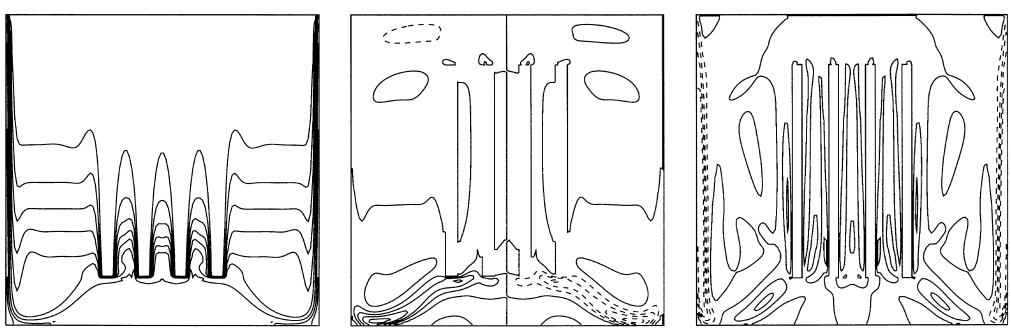

Figure 8. Steady state temperature and velocity fields for partitioned cavity at $Ra = 1.0 \times 10^8$, from left to right: temperature (isovalues are: 0.1, 0.2, 0.2, 0.4,0.5, 0.6, 0.7, 0.8, 0.9); horizontal and vertical velocities (isovalues are: 0, ± 0.05, ± 0.10, ± 0.15, ± 0.20).

For this Rayleigh number $Ra = 1.0 \times 10^8$, the average Nusselt number along each cold wall is 44.30. Assuming a classical laminar boundary layer scaling, the Nusselt number correlation is given by $Nu = 0.443 Ra^{1/4}$. This coefficient of proportionality is greater than that obtained for the differentially heated cavity. We note that the ratio between these two proportionality coefficients (0.44 versus 0.31) is almost the same as that between the maximum vertical velocity in the boundary layer (0.22 for the differentially heated cavity against 0.30 here).

5. DETERMINATION OF THE JACOBIAN SPECTRUM

5.1. General considerations

The stability of any steady solution U_0 to infinitesimal perturbations is investigated by letting any solution be written as $U_0 + \tilde{U}$, where $\tilde{U} = (\tilde{u}, \tilde{w}, \tilde{p}, \tilde{\theta})$ is the perturbation vector. Inserting this expression into the unsteady equations and neglecting second-order terms, yields

$$\frac{\partial \tilde{U}}{\partial t} = (L - DN_{U_0})\tilde{U} \tag{30}$$

where $(L - DN_{U_0}) = \mathscr{L}_{U_0}$ is the Jacobian of the Navier–Stokes equations evaluated at U_0.

Since $\mathscr{L}_{U_0}$ is independent of time, solutions to Equations (30) are of the form $\tilde{U}(x, z, t) = e^{\sigma t}\zeta(x, z)$. Inserting this expression into Equation (30) shows that $\zeta(x, z)$ is an eigenvector of the Jacobian $\mathscr{L}_{U_0}$ corresponding to the eigenvalue σ. Since $\mathscr{L}_{U_0}$ is real, its eigenvalues are either real or complex conjugates. If all eigenvalues have a negative real part the solution U_0 is linearly stable. If one eigenvalue at least is of positive real part then the solution U_0 is linearly unstable.

In bounded domains like those of interest here, the spectrum of the continuous Jacobian $\mathscr{L}_{U_0}$ consists of an infinite countable number of eigenmodes. After spatial discretization, the number of eigenmodes of the discrete Jacobian becomes finite and only part of these eigenmodes is a good approximation of those of the continuous Jacobian. It is therefore useless, if possible at all, to compute all the spectrum of the discrete Jacobian since the eigenvalues of interest for stability investigations are those of maximum real part. Computing these leading eigenvalues is far from trivial. As previously stated, when the configuration at hand requires large spatial discretization direct methods are not usable, and one has to resort to iterative methods, which generally consist in applying repeatedly some linear operator on a given initial vector. It is indeed well known that applying repeatedly an operator on a given initial vector will eventually polarize the resulting vector sequence along the eigenvector corresponding to the eigenvalue of largest modulus. Thus, in order to determine the eigenvalues of maximum real part of the Jacobian, the general technique is to apply power iterate methods with a function of the Jacobian that will turn the leading eigenvalues of interest into those of maximum modules of the function of the Jacobian (see [23]). The best candidate for this is obviously the exponential of the Jacobian but as previously stated this cannot be done in practice and one has to use an approximation of the exponential such as $(I + \delta t \mathscr{L}_{U_0})$ with $\delta t \ll 1$. Another possible candidate is an inverse power iterate with a shift that will make the eigenmode closest to the shift dominant [24,25]. This method was successfully applied for real shifts [24], but still suffers from some unresolved problems for complex shifts [25].

We have used the ARPACK library developed by Sorensen [26] and Lehoucq [27] with the technique described just above to compute several eigenvalues and the corresponding eigenmodes. The ARPACK library [10] works on the basis of an Arnoldi–Krylov algorithm, where an invariant subspace of specified dimension is determined through the repeated action of an operator acting on a sequence of vectors. It offers the possibility to specify the desired eigenmodes, such as those of maximum real part or those of maximum modulus. We have tried

two possibilities: either using directly the Jacobian $\mathscr{L}_{U_0}$ requiring the eigenvalues of maximum real part or using $I + \delta t \mathscr{L}_{U_0}$ (where the time step δt has been set to $\simeq 10^{-3}$), requiring the eigenvalues of maximum modulus.

In either case, the explicit action of the Jacobian on a given vector was performed in two steps. In the first step, the spatial part was computed explicitly, i.e. the discretized form of the operator $-U_0\nabla\cdot - \cdot\nabla U_0 + \nabla^2$ was applied on a vector consisting of $(\tilde{u}, \tilde{w}, \tilde{\theta})$. In matrix notation this reads

$$\begin{pmatrix} -\bar{u}\dfrac{\partial}{\partial x} - \bar{w}\dfrac{\partial}{\partial z} - \cdot\dfrac{\partial \bar{u}}{\partial x} + \dfrac{Pr}{\sqrt{Ra}}\nabla^2 & -\cdot\dfrac{\partial \bar{u}}{\partial z} & 0 \\ -\cdot\dfrac{\partial \bar{w}}{\partial x} & -\bar{u}\dfrac{\partial}{\partial x} - \bar{w}\dfrac{\partial}{\partial z} - \cdot\dfrac{\partial \bar{w}}{\partial z} + \dfrac{Pr}{\sqrt{Ra}}\nabla^2 & Pr \\ -\cdot\dfrac{\partial \bar{\Theta}}{\partial x} & -\cdot\dfrac{\partial \bar{\Theta}}{\partial z} & -\bar{u}\dfrac{\partial}{\partial x} - \bar{w}\dfrac{\partial}{\partial z} + \dfrac{1}{\sqrt{Ra}}\nabla^2 \end{pmatrix} \begin{pmatrix} \tilde{u} \\ \tilde{w} \\ \tilde{\theta} \end{pmatrix}$$

This step is followed by a projection step in which the resulting velocity field is projected onto the space of divergence free vector fields. This projection $\mathscr{P}$ reads $\mathscr{P} = I - \nabla(\nabla\cdot\nabla)^{-1}\nabla\cdot$ and is performed through a scalar multigrid algorithm for the computation of the pressure.

Either evaluation thus reads $\mathscr{P}\mathscr{M}_{U_0}$ or $\mathscr{P}(I + \delta t \mathscr{M}_{U_0})$, where $\mathscr{M}_{U_0}$ stands for the matrix just above. We have found that the use of $\mathscr{P}(I + \delta t \mathscr{M}_{U_0})$ requiring the eigenvalues of maximum modulus works much better than the other alternative. Note that this is equivalent to performing an explicit time stepping of the linearized Navier–Stokes equations. The reason why we have not used a straightforward modification of the implicit–explicit time stepping scheme (23) is that the corresponding time stepping scheme would not be a polynomial of $\mathscr{L}_{U_0}$. Although the eigenvalues would yield good approximations, the corresponding eigenvector would not be exactly those of $\mathscr{L}_{U_0}$ and this is important for a later purpose.

5.2. Differentially heated cavity

We have validated the above procedure on the case of the differentially heated cavity of aspect ratio 4 which has been extensively studied in the past [12]. In particular the critical Rayleigh number was determined to be very close to 1.03×10^8 ($Ra_W = 1.61 \times 10^6$). This was determined from the theoretical relationship relating the amplitude of the oscillations to the difference $Ra - Ra_c$ in the case of a supercritical Hopf bifurcation. The finite amplitude solutions were obtained with a two-dimensional Chebyshev code and enough resolution was used (40×96) so that spatial convergence was obtained.

We have computed the 100 most unstable eigenmodes of the Jacobian for $Ra = 1.024 \times 10^8$ ($Ra_W = 1.6 \times 10^6$) for three different spatial resolutions consisting of an uniform mesh of 64×128, 128×256 and 256×256. As Figure 9 shows, the most unstable modes of the spectrum shift to the right as the spatial resolution is increased. This means that a too coarse spatial resolution makes the steady state solution too stable. In fact, for a spatial resolution of 64×128, the solution becomes unstable for a Rayleigh value slightly above $Ra = 1.28 \times 10^8$

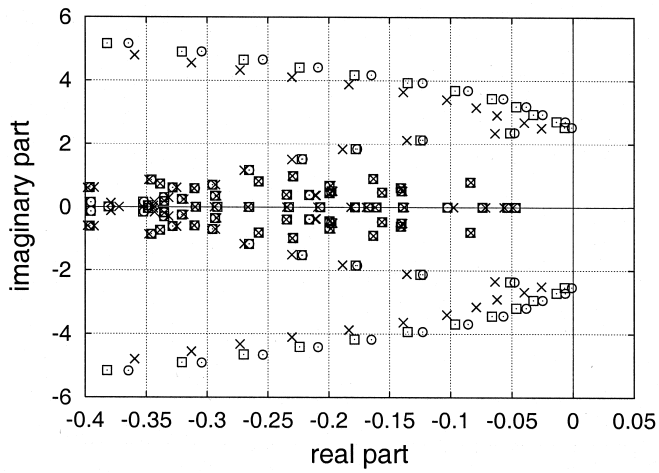

Figure 9. Jacobian spectrum for differentially heated cavity at $Ra = 1.024 \times 10^8$ for three meshes: $\times$, 64×128; $\square$, 128×256; $\bigcirc$, 256×256.

(20 per cent too large), whereas for 128×256, the solution becomes unstable for a Rayleigh value approximately equal to $Ra = 1.13 \times 10^8$ (still 10 per cent too large). It should be noted that the imaginary parts of the eigenvalues seem almost completely unsensitive to an under resolution as are some eigenvalues of small imaginary part. Note also that the spatial structure of the eigenmodes, which will be discussed in more detail below, did not change qualitatively for the three spatial resolutions.

For the larger spatial resolution of 256×256, the spectrum (which of course required the computation of the corresponding steady state solution) was computed for two values of Ra, 1.024×10^8 and 1.056×10^8 (Ra_W of 1.6×10^6 and 1.65×10^6). Figure 10 presents the corresponding spectra, showing that the solution has become linearly unstable for the larger Rayleigh value. It should also be noted that the eigenvalues of large imaginary part (larger than the critical one) move fastest to the right as the Rayleigh number is increased. This is evidenced in Figure 11, which presents the evolution of the real part for the corresponding eigenvalues. This figure also shows that the most unstable eigenvalue crosses the imaginary axis for approximately 1.035×10^8, a value that differs by less than 1 per cent from the previously determined critical value.

All these eigenvalues and corresponding eigenmodes were obtained requiring the 100 eigenmodes of largest modulus of $\mathscr{P}(I + \delta t \mathscr{M}_{U_0})$. Parameter studies showed that the optimal time step was 10^{-3}. Obtaining the 100 eigenmodes required in general between 30 000 and 50 000 evaluations of this operator.

As just stated, the above results were obtained with the use of $\mathscr{P}(I + \delta t \mathscr{M}_{U_0})$ requiring a given number of eigenmodes of maximum modulus. Since there is no guarantee that some modes have not been overlooked, and second that the ordering on the modulus carries over to the real parts, we performed several tests, requiring an increasing number of eigenmodes,

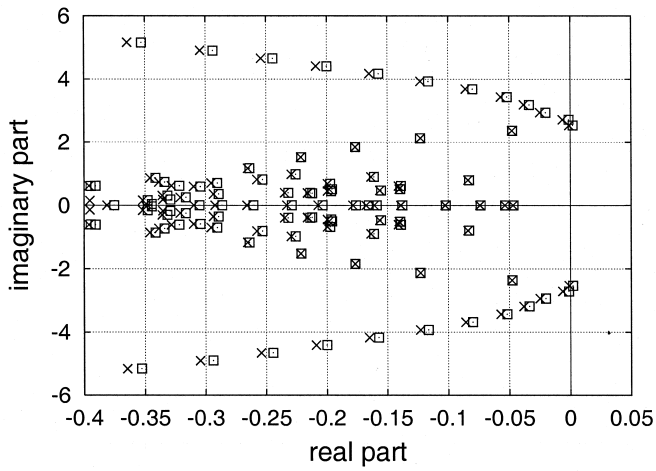

Figure 10. Jacobian spectrum for differentially heated cavity for a 256×256 mesh: $\times$, $Ra = 1.024 \times 10^8$; $\square$, $Ra = 1.056 \times 10^8$.

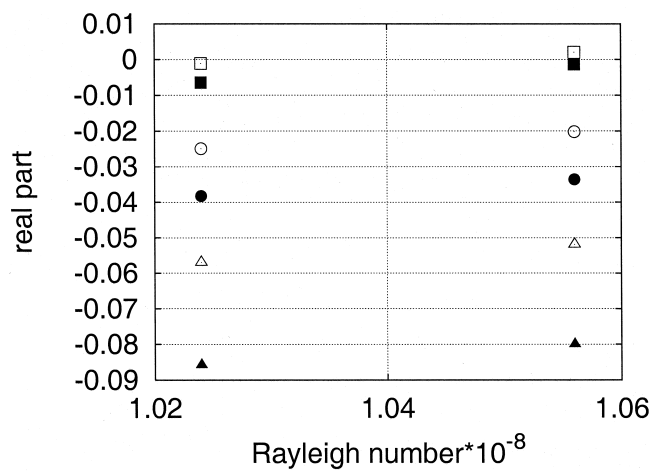

Figure 11. Real part of the most unstable eigenmodes with large imaginary part for differentially heated cavity at $Ra = 1.024 \times 10^8$ and $Ra = 1.056 \times 10^8$ for a 256×256 mesh.

namely 100, 200, 300 and 400. The results are plotted in Figure 13 and it can be seen that essentially the eigenvalues are determined in decreasing order of their real parts (for computing limitations this test was performed for the lowest spatial resolution of 64×128).

We now illustrate the dependence of the spectrum over a larger range of Rayleigh values. For computing limitations, these results were obtained with a spatial resolution of 128×256.

Figure 12 shows the spectrum of the Jacobian for four Rayleigh numbers of 1.024×10^8, 1.28×10^8, 1.6×10^8 and 1.92×10^8 (i.e. Ra_W of 1.6×10^6, 2×10^6, 2.5×10^6 and 3×10^6). When the Rayleigh number increases, the Jacobian spectrum globally shifts to the right. While for 1.024×10^8 the solution is still linearly stable, the number of unstable modes increases with Rayleigh number: three for $Ra = 1.28 \times 19^8$; five for $Ra = 1.6 \times 10^8$ and six for $Ra = 1.92 \times 10^8$. Note that most eigenvalues, at least those of large imaginary part, move parallel to the real axis, which was not the case for the spectrum of the square cavity with conducting walls computed by Winters [28]. This is due to the fact that the reference time used here is the convective time scale, whereas Winters used a thermal diffusion time scale. The present choice thus allows one to follow the eigenvalues, which depend continuously on the Rayleigh number, more easily. In particular, it is to be noted that because of the fact that the real part of the eigenvalues moves fastest to the right for increasing imaginary part, it is not the critical eigenmode (i.e. the first one to become unstable) that will remain the most unstable one (that of largest real part) as the Rayleigh number increases. This is to be related to the existence of multiple branches of unsteady solutions as described in [12]. Note also, however, that not all the eigenvalues move to the right as the Rayleigh number is increased and some modes become more stable (those of imaginary part close to 2, for example).

Let us analyse in more detail the 400 more unstable eigenmodes of the spectrum of the Jacobian for $Ra = 1.6 \times 10^8$ (Figure 13). This represents a considerable amount of information and we only discuss here their salient features. The eigenmodes can be, at first glance, divided in three groups. One group corresponds to complex conjugate eigenvalues of large imaginary part. Starting from the upper left corner, the real part increases at first when the imaginary part decreases, until the eigenvalues cross the imaginary axis. The curve turns around, the real part decreasing upon further decrease of the imaginary part. The second group of eigenvalues

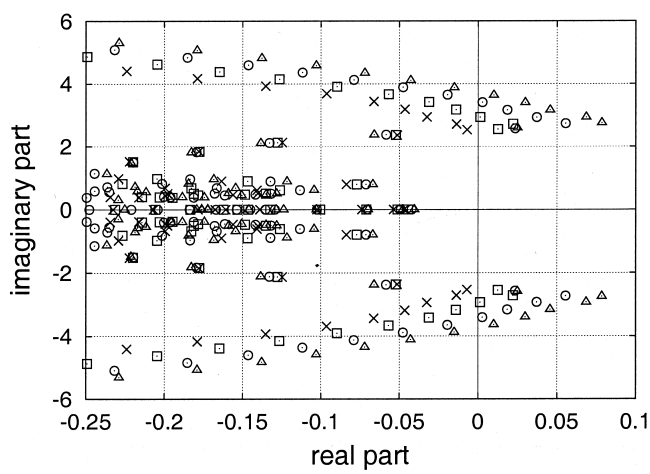

Figure 12. Jacobian spectrum for differentially heated cavity for a 128×256 mesh: $\times$, $Ra = 1.024 \times 10^8$; $\square$, $Ra = 1.28 \times 10^8$; $\bigcirc$, $Ra = 1.6 \times 10^8$; $\triangle$, $Ra = 1.92 \times 10^8$.

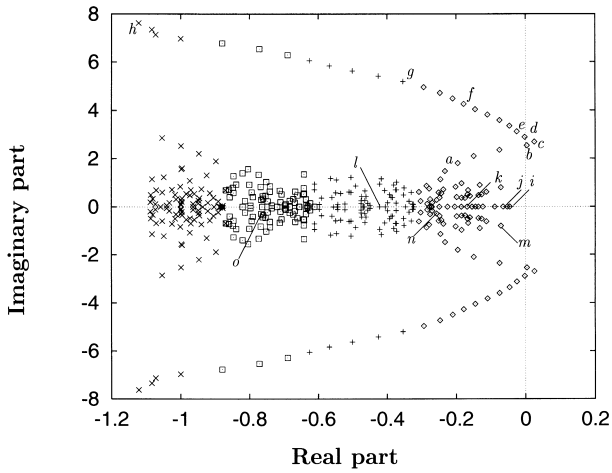

Figure 13. Jacobian spectrum for differentially heated cavity at $Ra = 1.6 \times 10^8$ for a 64×128 mesh: $\diamondsuit$, 100 first eigenmodes required; $+$, 100 more eigenmodes; $\square$, 100 more eigenmodes; $\times$, 100 more eigenmodes.

is the real ones. The third group is the rest, those of imaginary part of order one or less, for which no distinctive classification criteria show up. Sample eigenmodes for each group are given in Figure 14 (we just show the temperature component of the eigenmodes, and just its real part in the case of complex eigenmodes). Eigenmodes labelled by letters a–h correspond to the first group, those from i to l to the second and m–o to the third. The first group of eigenmodes is clearly boundary layer modes, as evidenced by the fact that the amplitude in the core region is very close to zero. Each mode has a well-defined number of structures (we define a structure as the association of two consecutive patches of alternate sign), starting from eight for mode c and increasing sequentially. Modes d, e, f, g and h correspond to 9, 10, 15, 19 and 30 structures respectively. Conversely, the number of structures of boundary layer modes of decreasing imaginary part decreases sequentially, seven for mode b and four for mode a. Modes i–l are steady modes. These modes will correspond to the deformation of the base flow due to the time-averaged values of the interactions of the non-linear terms. As can be seen from their structure, some modes (like i and j) correspond to deformation of the end regions, whereas others (like k and l) correspond to changes in the mean stratification of the core region. Lastly, the third group mostly consists of oscillating internal wave modes. This is consistent with the Brunt Väisälä cut-off frequency based on a mean core stratification of $C(\Delta T/H)$ which is, in our time units, $\sqrt{CPr}$. Modes of imaginary parts close to this value ($\simeq 0.85$) (mode m) display a vertical structure whereas those of imaginary part close to zero (modes n and o) display a quasi-horizontal structure, in agreement with the classical dispersion relationship [29].

The well-known centrosymmetry of the base flow (skew-symmetry for both velocity components and temperature and symmetry for pressure) results in eigenmodes that either share this

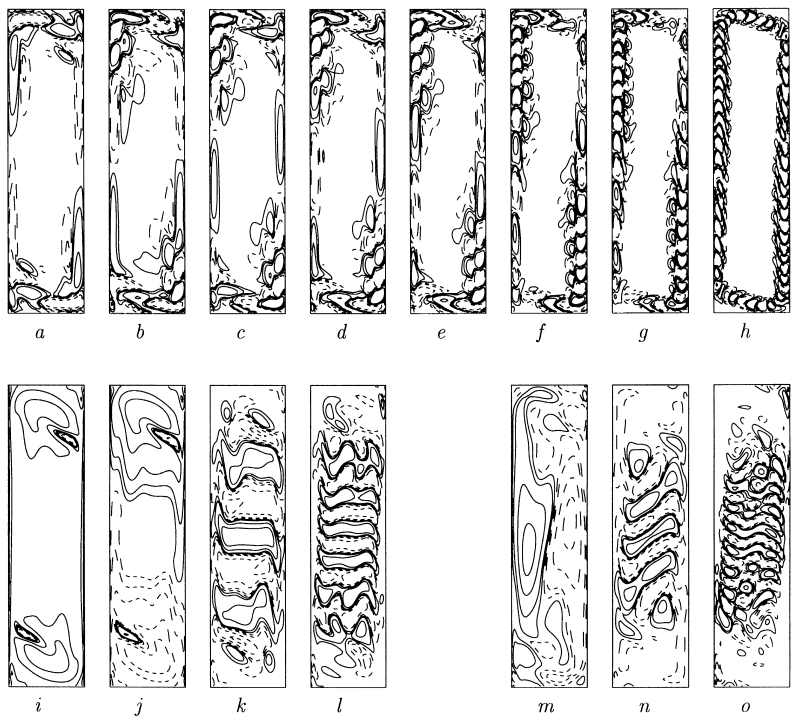

Figure 14. Selected eigenmodes for differentially heated cavity at $Ra = 1.6 \times 10^8$ (letters refer to Figure 13).

property or possess the opposite symmetry (symmetry for the velocity components and temperature and skew-symmetry for pressure). For the boundary layer modes, those that have an odd number of structures have the symmetry of the base flow, whereas those with an even number of structures have the opposite symmetry. The most unstable eigenmode for $Ra = 1.6 \times 10^8$ is a boundary layer mode characterized by 8 structures (eigenmode *c* in Figure 14) and an imaginary part of 2.69, corresponding to a period of 2.33 (in convective time units). This is in good agreement with the second branch of solutions found in full non-linear simulations [12].

5.3. Cavity with internal plates

We have computed the spectrum of the Jacobian in the partitioned cavity for a Rayleigh number of $Ra = 1.0 \times 10^8$ with a uniform mesh of 256×256. The computation of the 100 eigenmodes of largest modulus of $\mathscr{P}(I + \delta t \mathscr{M}_{U_0})$ required about 90 000 evaluations of this operator.

The spectrum is displayed in Figure 15 and some characteristic eigenmodes are shown in Figure 16. For $Ra = 1.0 \times 10^8$, the flow is stable and all eigenvalues have negative real parts.

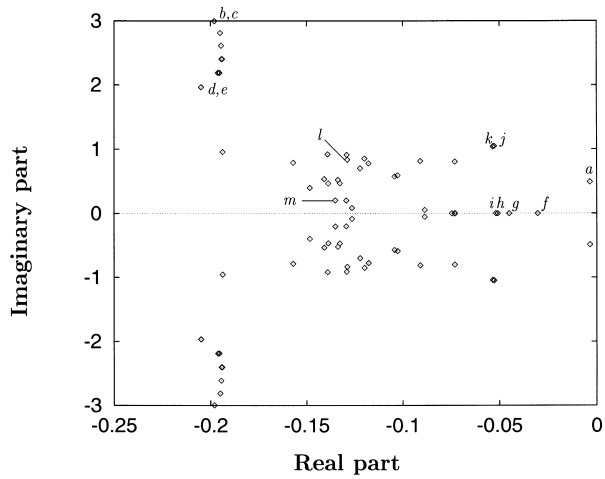

Figure 15. Jacobian spectrum for partitioned cavity of $Ra = 1.0 \times 10^8$.

The most unstable eigenmode corresponds to a complex eigenvalue with a barely negative real part. This will be the first eigenmode to become unstable when increasing *Ra*. It is anti-symmetrical with respect with the median vertical axis (anti-symmetry for the temperature and the horizontal velocity, symmetry for the vertical velocity and the pressure) and the maximum of fluctuations is located just below the outer plates (eigenmode *a* in Figure 16). The imaginary part of the eigenvalue corresponds to a period of 12.7, which is in agreement with the fluctuating temperature field obtained as time-periodic solution of the non-linear problem for Rayleigh number values just above the critical threshold [22].

Due to the geometry and boundary conditions, the base flow is symmetrical with respect to the cavity vertical mid plane (symmetry for temperature, vertical velocity and pressure, anti-symmetry for horizontal velocity). As a consequence all the eigenmodes either share this property or have the opposite symmetry (anti-symmetry for temperature, vertical velocity and pressure, symmetry for horizontal velocity). Some eigenvalues are found nearly superposed, corresponding to almost degenerate eigenmodes, one of them corresponding to a symmetric eigenmode the other to an anti-symmetric one of similar structure.

As was done for the differentially heated cavity, the spectrum can be divided in three similar groups: one group for the complex conjugate eigenvalues of large imaginary part, a second group for the real eigenvalues, and the rest. The eigenvalues with large imaginary part (e.g. greater than 2.0 here) correspond to channel instability eigenmodes as their amplitudes are maximum there (eigenmodes *b*, *c*, *d*, *e* in Figure 16). In fact, each point is a nearly double eigenvalue corresponding to two almost degenerate eigenmodes: one is symmetric and the other is anti-symmetric. Each eigenmode corresponds to a well-defined

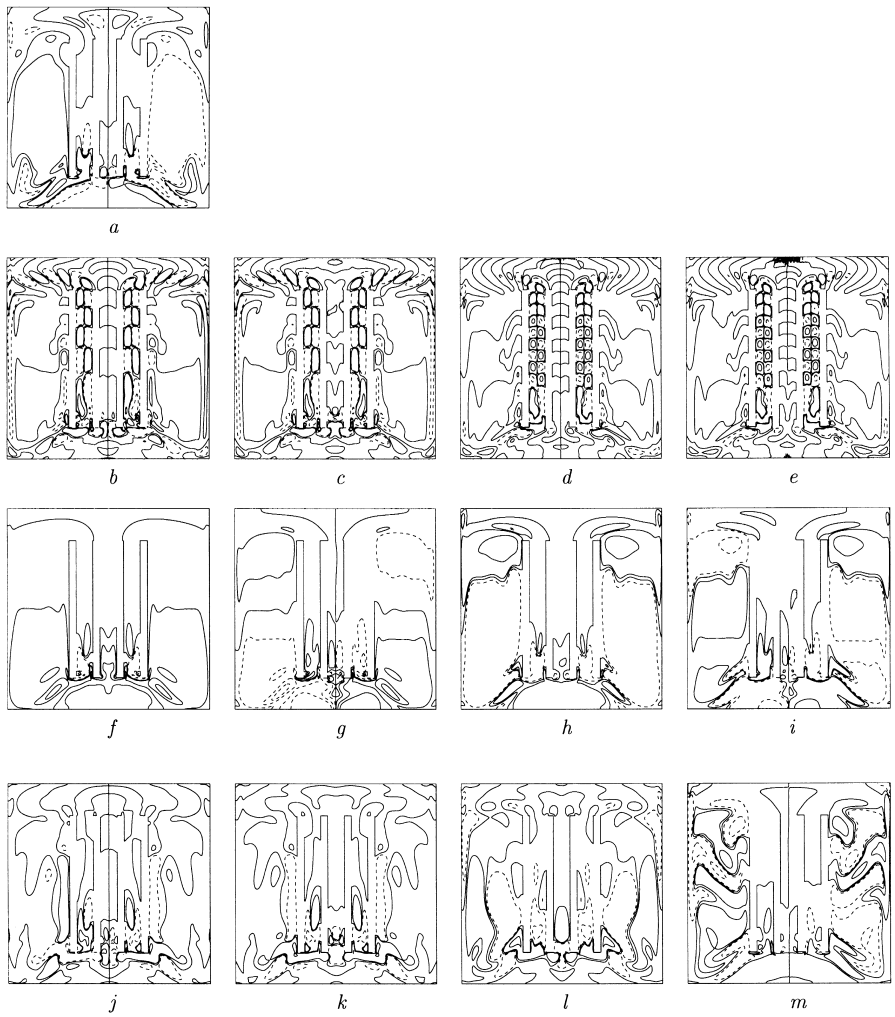

Figure 16. Selected eigenmodes for partitioned cavity at $Ra = 1.0 \times 10^8$ (letters refer to Figure 15).

number of structures circulating around the cavity starting from eight for modes *b* and *c* to 13 for modes *d* and *e*. Modes *f*–*i* are steady modes. Some of them correspond to deformation in the recirculating zones at the bottom of the lower boundary layers (eigenmodes *f* and *g* in Figure 16), others affect the thermally stratified part outside the channels (modes *h* and *i*). Here again, symmetric and anti-symmetric eigenmodes are around close to one another. For the last group, eigenmodes correspond to oscillating modes with maximum amplitude standing either at the bottom of the chimneys (modes *j* and *k*) or instead in the thermally stratified zone outside the internal plates (modes *l* and *m*).

6. DETERMINATION OF THE ADJOINT JACOBIAN SPECTRUM

6.1. General considerations

Our motivation for computing the spectrum and eigenvectors of the adjoint of the Jacobian is twofold. Firstly, it is known that the eigenmodes of the adjoint contain the spatial information concerning the localization of the maximum sensitivity of the corresponding eigenmode of the Jacobian [11,30]. This has obvious implications in active control, where it is important to determine the optimum localization of forcing terms. Our second motivation is to develop a method to reduce the Navier–Stokes equations to a low-order differential system able to represent the dynamics of the flow at low cost [31,32]. This also has obvious applications in active control in order to dispose of a fast predictive dynamical model that one can use in a feedback loop. To this aim, we propose to express the solution $U(x, z, t)$ of the Navier–Stokes equations at a given Rayleigh number as

$$U(x, z, t) = U_0(x, z) + \tilde{U}(x, z, t) \tag{31}$$

where $U_0(x, z)$ is the stable or unstable steady solution for the given Rayleigh number. The non-linear Navier–Stokes equations can then be written as

$$\frac{\partial \tilde{U}}{\partial t} = (L - DN_{U_0})\tilde{U} - \tilde{U} \cdot \nabla \tilde{U} \tag{32}$$

$$= \mathscr{L}_{U_0}\tilde{U} - \tilde{U} \cdot \nabla \tilde{U} \tag{33}$$

We decompose $\tilde{U}(x, z, t)$ into the form

$$\tilde{U}(x, z, t) = \sum_k A_k(t)\zeta_k(x, z) \tag{34}$$

where the $\zeta_k(x, z)$s are selected eigenvectors of the Jacobian $\mathscr{L}_{U_0}$ and the $A_k(t)$s are then the expansion coefficients. Inserting this expansion into the non-linear Navier–Stokes equations yields

$$\sum_k \frac{\mathrm{d}A_k(t)}{\mathrm{d}t}\zeta_k(x, z) = \sum_k \sigma_k A_k(t)\zeta_k(x, z) - \sum_{l,m} A_l A_m \zeta_l(x, z) \cdot \nabla \zeta_m(x, z) \tag{35}$$

where σ_k is the eigenvalue corresponding to $\zeta_k(x, z)$.

In order to arrive at the differential system, one must take the inner product of Equation (35) with a set of $\xi_i(x, z)$ which is bi-orthogonal to $\zeta_k(x, z)$ i.e.

$$(\xi_i(x, z), \zeta_k(x, z)) = \delta_{ik} \tag{36}$$

where $(f, g) = \int \bar{f} g$ is the hermitian inner product. Since $\mathscr{L}_{U_0}$ is not self-adjoint, its eigenmodes are not orthogonal, and the bi-orthogonal set are the eigenmodes $\xi_k(x, z)$ of the adjoint of the Jacobian. Upon taking the inner product of Equation (35) with $\xi_k(x, z)$, one obtains the non-linear differential system

$$\frac{\mathrm{d}A_k}{\mathrm{d}t} = \sigma_k A_k - \sum_{l,m} \mu_{klm} A_l A_m \tag{37}$$

where $\mu_{klm} = (\xi_k(x, z), \zeta_l(x, z) \cdot \nabla \zeta_m(x, z))$. Note that this expression is exact and does not depend on any assumption related to the amplitude of the coefficients.

The adjoint operator is defined relative to the inner product $(f, g) = \int \bar{f} g$ such that

$$(V, \mathscr{L} U) = (\mathscr{L}^* V, U) \tag{38}$$

We recall here that $\mathscr{L}$ and $\mathscr{L}^*$ are characterized by the same set of eigenvalues. In expanded form, the definition of the adjoint $\mathscr{M}^*_{U_0}$ for the spatial part $\mathscr{M}_{U_0}$ reads

$$(\tilde{u}^* \quad \tilde{w}^* \quad \tilde{\theta}^*)(\mathscr{M}_{U_0}) \begin{pmatrix} \tilde{u} \\ \tilde{w} \\ \tilde{\theta} \end{pmatrix} = (\tilde{u} \quad \tilde{w} \quad \tilde{\theta})(\mathscr{M}^*_{U_0}) \begin{pmatrix} \tilde{u}^* \\ \tilde{w}^* \\ \tilde{\theta}^* \end{pmatrix} \tag{39}$$

Using integration by part and invoking the fact that the velocity fields are divergence free, $\mathscr{M}^*_{U_0}$ can be written in continuous form as

$$\begin{pmatrix} \bar{u}\dfrac{\partial}{\partial x} + \bar{w}\dfrac{\partial}{\partial z} - \cdot\dfrac{\partial \bar{u}}{\partial x} + \dfrac{Pr}{\sqrt{Ra}}\nabla^2 & -\cdot\dfrac{\partial \bar{w}}{\partial x} & -\cdot\dfrac{\partial \bar{\Theta}}{\partial x} \\ -\cdot\dfrac{\partial \bar{u}}{\partial z} & \bar{u}\dfrac{\partial}{\partial x} + \bar{w}\dfrac{\partial}{\partial z} - \cdot\dfrac{\partial \bar{w}}{\partial z} + \dfrac{Pr}{\sqrt{Ra}}\nabla^2 & -\cdot\dfrac{\partial \bar{\Theta}}{\partial z} \\ 0 & Pr & \bar{u}\dfrac{\partial}{\partial x} + \bar{w}\dfrac{\partial}{\partial z} + \dfrac{1}{\sqrt{Ra}}\nabla^2 \end{pmatrix}$$

Note that this form clearly shows that the transport by the steady flow in $\mathscr{M}^*_{U_0}$ takes place in the opposite direction.

6.2. Numerical implementation

It would be tempting to discretize directly the above operator, which would then be used like in the direct method, followed by a projection step to extract the divergence part of the velocity. This is not the correct way to proceed since for the adjoint eigenmodes $\xi_i(x, z)$ to be orthogonal to the $\zeta_k(x, z)$s, the $\xi_i(x, z)$s must be the eigenmodes of the *adjoint of the discrete Jacobian* that was used to compute the eigenmodes $\zeta_k(x, z)$s [33]. There are thus two issues

related to this difficulty. One is linked to the sequence in which these two steps are performed while the other is linked to the spatial discretization itself.

Assume for instance that the eigenmodes of the Jacobian have been computed using the operator $\mathscr{P}(I+\delta t\mathscr{M}_{U_0})$. The formal adjoint of this operator is $(I+\delta t\mathscr{M}^*_{U_0}))\mathscr{P}^t$ where the superscript t indicates transposition and it is the vector that comes from the action of the above operator on a previous iterate that has to be used to built the Krylov subspace.

Let us now deal with the spatial discretization. It is known that the Laplacian is self-adjoint with respect to the weighted inner product

$$(f, g)_d = \sum_i \overline{f(x_i)} g(x_i)\, \mathrm{d}x_i$$

where $\mathrm{d}x_i$ is the mesh size, even non-uniform. As for the non-linear terms, let us briefly illustrate the computation of the discrete adjoint, for the temperature field for instance. The classical space-centered expression resulting from the finite volume integration of the convective term in conservative form $\partial u\theta/\partial x$ used for the Jacobian reads, with standard notations

$$\bar{u}_{i+1/2}\frac{\tilde{\theta}_{i+1}+\tilde{\theta}_i}{2} - \bar{u}_{i-1/2}\frac{\tilde{\theta}_i+\tilde{\theta}_{i-1}}{2} \tag{40}$$

Multiplying this equation by $\tilde{\theta}^*_i$ and shifting indices to factor out $\tilde{\theta}_i$ results in the discret adjoint form of the convective terms

$$\frac{\bar{u}_{i+1/2}(\tilde{\theta}^*_{i+1}-\tilde{\theta}^*_i) + \bar{u}_{i-1/2}(\tilde{\theta}^*_i-\tilde{\theta}^*_{i-1})}{2} \tag{41}$$

which is merely the average value of the convective form $u(\partial\theta^*/\partial x)$ of the transport term evaluated at $x_{i+1/2}$ and $x_{i-1/2}$.[3] Similar although more complex expressions, in particular on non-uniform meshes, can be derived for the convective terms of the momentum equations.

As for the projection $\mathscr{P}$, it is easy to see that it is self adjoint since, loosely speaking, $(\nabla)^t = -(\nabla\cdot)$. This demonstration requires appropriate functional analysis. It is guaranteed here because the use of the staggered grid arrangement yields pressure and velocity fields in compatible vector spaces.

The adjoint eigenmodes were also computed using the ARPACK library. Requesting the same number of modes of largest modulus yielded the same set of eigenvalues as for the direct problem. The eigenvalues were found equal to within 10^{-10} and the two spectra can be superposed. There modes are defined to within a rotation in the complex plane (if $\xi_k(x,z)$ is an eigenmode, $\exp(\mathrm{i}\phi)\xi_k(x,z)$ is also an eigenmode). Although the two sets computed by ARPACK are indeed bi-orthogonal, appropriate rotations were applied to the adjoint eigenmodes in order to satisfy the orthonormality condition (36). For a set of almost 400

[3] Note that this expression is not conservative. As a consequence, the celebrated skew-symmetric form of the convective term, which is half the sum the of expressions (40) and (41), and reads $\bar{u}_{i+1/2}\tilde{\theta}_{i+1} - \bar{u}_{i-1/2}\tilde{\theta}_{i-1}$; although it conserves $\tilde{\theta}^2$ at the discrete level does no longer conserve $\tilde{\theta}$!

eigenmodes for the Jacobian and as many for the adjoint problem, the inner products are equal to 1 or 0 with a precision better than 10^{-10}.

6.3. Differentially heated cavity

As a representative example, we have chosen to present in Figure 17 the eigenmodes of the adjoint Jacobian spectrum corresponding to those displayed in Figure 13, for $Ra = 1.6 \times 10^8$.

As can be seen, the adjoint eigenmodes that correspond to the direct boundary layer modes also have their maximum amplitude in the boundary layers. It can be seen that they have the same number of structures that their corresponding direct eigenmodes. Note, however, that these adjoint modes have their maximum amplitude in the bottom part of the upward boundary layer and symmetrically in the upper part of the downward boundary layer. One can conclude that the receptivity of the boundary layer modes will be maximum if they are forced in the upstream part of the boundary layer at approximately one-third from the starting corner.

These computations are thus in agreement with the intuitive feeling that boundary layer modes should be preferably forced at the beginning of the boundary layer. Note however that

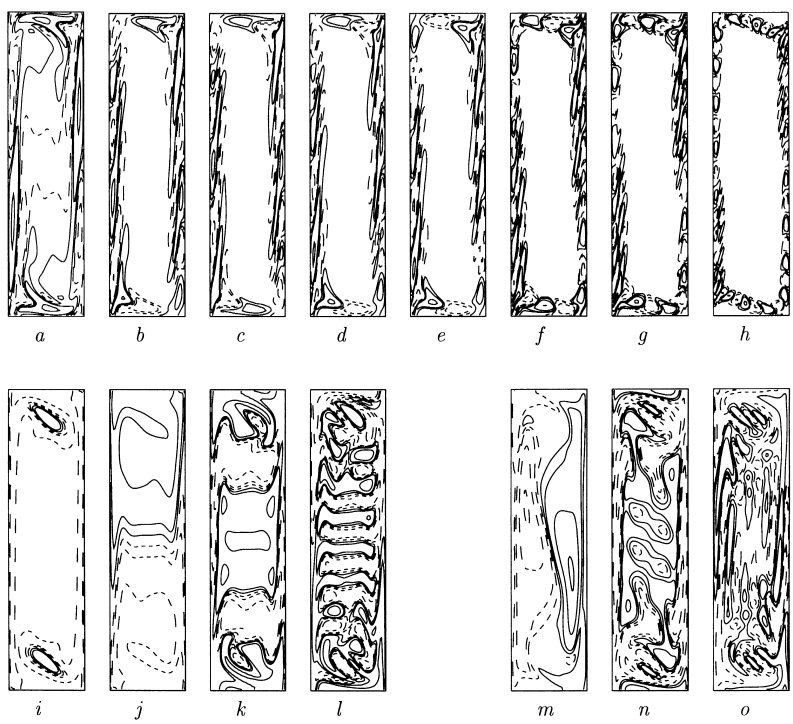

Figure 17. Selected adjoint eigenmodes for differentially heated cavity at $Ra = 1.6 \times 10^8$ (letters refer to Figure 13).

in more complex situations like the cavity with internal plates, in which the most unstable mode is not a boundary layer mode, it is the computation of the adjoint eigenmodes that has enabled us to find the optimal location of forcing. These experiments are reported in [22].

6.4. Example of low-order dynamical system

The adjoint eigenmodes can be used to compute the coefficients

$$\mu_{klm} = (\xi_k(x, z), \zeta_l(x, z) \cdot \nabla \zeta_m(x, z))$$

which appear in the non-linear ordinary differential equations. We have performed these computations for a Rayleigh number value of 6.4×10^7 in the aspect ratio 4 cavity, that is when the steady solution is still stable, using the 100 modes of largest real part as expansion basis. The differential system (37) was integrated using the same time discretization scheme (second-order backwards Euler for the time derivative coupled to explicit Adams–Bashforth for the non-linear terms) as that used for the full Navier–Stokes equations. The Navier–Stokes equations were integrated in fluctuating form, starting from a random initial field of small amplitude. The initial values for the coefficients of the differential system were obtained from the projection of the random field on the expansion basis, which is done by taking the inner product of this random field with the adjoint eigenmodes.

Figure 18 shows the comparison of the fluctuating temperature at a given monitoring point between the full non-linear equations and the synthesized temperature corresponding to the differential system during the transient leading back to steady state. Both signals are virtually undistinguishable except for very small times when the high frequency of the initial condition is not adequately represented on the eigenmodes expansion basis. Work is in progress in the unstable case.

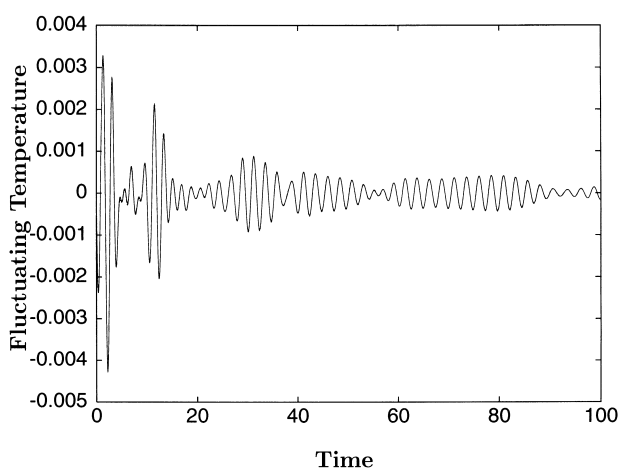

Figure 18. Time trace of fluctuating temperature for differentially heated cavity at $Ra = 6.4 \times 10^7$; non-linear computation, full line; dynamical model, dashed line.

7. CONCLUSIONS

We have presented a general methodology for the investigation of the stability of natural convection flows in enclosures of complex geometry. This methodology consists of a steady state solver and of algorithms to compute the leading part of the spectrum of the Jacobian on a steady state solution and that of the adjoint of the Jacobian. We have implemented the steady state solver based on Newton's iterations with the help of a Stokes solver based on an iterative multigrid algorithm, which is capable of handling both rectangular and complex geometries, such as a cavity with internal plates. We have been able to follow the steady solution in a differentially heated cavity of vertical aspect ratio 4 for Rayleigh values more than one order of magnitude above the critical value. This has allowed us to confirm the asymptotic structure of the boundary layer regime.

Computation of the leading eigenmodes, those of largest real part of the Jacobian was performed through the use of the ARPACK library. We have shown that provided spatial resolution is used the critical Rayleigh number thus determined agrees very well with the accurate determination previously performed using a time dependent code using Chebyshev collocation. The advantage of this new approach is the possible computation of several hundred eigenmodes. In the differentially heated cavity the oscillating eigenmodes can be classified into boundary layer modes and internal wave modes. In the cavity with internal partitions, oscillating channel modes have been found. Due to the base flow symmetry, some nearly degenerate eigenvalues have been found which correspond to modes with different symmetries.

Care was taken to compute the eigenmodes of the adjoint of the discrete Jacobian, in order to ensure the orthogonality of the two sets to within machine accuracy. This allowed us to build a low-order dynamical system by expanding the unsteady solution as the sum of the steady state solution and of a linear combination of selected eigenmodes. The comparison of the time evolution of the full non-linear computation with the solution of the differential system was excellent in a stable case.

We are confident that this general methodology will prove useful in understanding transition to unsteadiness and chaos of internal flows as well as for controlling them.

ACKNOWLEDGMENTS

We have benefited from many stimulating discussions with Drs J.L. Guermond, L.S. Tuckerman and S. Xin. We would like to thank Drs D.C. Sorensen and R.B. Lehoucq for providing a copy of the ARPACK library. The computations were performed on a C90 at IDRIS and on an SGI O2K located at CRIHAN. This work was carried out in the framework of the AMETH program.

APPENDIX A. NOMENCLATURE

A_κ	expansion coefficient
C	thermal stratification
g	acceleration of gravity
H	height of the enclosure

ℓ	width of the enclosure
$\mathscr{L}_{U_0}$	Jacobian of the Navier–Stokes operator evaluated on U_0
$\mathscr{M}_{U_0}$	spatial part of the Jacobian of the Navier–Stokes operator evaluated on U_0
$\mathbf{n}$	outward normal
Nu	average Nusselt number, reference heat flux is $\lambda(T_2 - T_1)/H$
P	dimensionless deviation from the hydrostatic pressure
$\mathscr{P}$	projection operator
Pr	Prandtl number, v/κ
Ra	width based Rayleigh number, $= g\beta\Delta T H^3/v\kappa$
Ra_{W}	width based Rayleigh number, $= g\beta\Delta T \ell^3/v\kappa$
R_F	aspect ratio of the enclosure, H/L
t	dimensionless time
T	dimensional temperature
T_1	cold wall temperature
T_2	hot wall temperature
U_0	steady state
U^k	current iterate
$\tilde{U}$	vector of perturbations
w (u)	vertical (horizontal) component of dimensionless velocity
x (z)	dimensionless co-ordinates, x^*/H (z^*/H)

Greek symbols

β	coefficient of volumetric thermal expansion
δ_{Ik}	Kronecker symbol
δt	time step
ϕ	press increment
κ	thermal diffusivity
λ	thermal conductivity
v	kinematic viscosity
σ_k	eigenvalue of the Jacobian $\mathscr{L}_{U_0}$
ξ_k	eigenvector of the adjoint of the Jacobian $\mathscr{L}_{U_0}$
ζ_k	eigenvector of the Jacobian $\mathscr{L}_{U_0}$
ΔT	temperature difference between walls, $T_2 - T_1$
ΔU^k	increment, $= U^{k+1} - U^k$
Θ	dimensionless temperature, $\Theta = (T - T_1)/\Delta T$

REFERENCES

1. Cliffe KA. Numerical calculations of two-cell and single-cell Taylor flows. *Journal of Fluid Mechanics* 1983; **135**: 219–233.
2. Tuckerman LS. Steady-state solving via Stokes preconditioning: Recurrence relations for elliptic operators. In *Lecture Notes in Physics*, Dwoyer DL, Hussaini MY, Voigt RG (eds). Springer: New York, 1989; 573–577.
3. Mamum CK, Tuckerman LS. Asymmetry and Hopf bifurcation in spherical Couette flow. *Physics of Fluids* 1995; **7**: 80–91.
4. Xin S, Le Quéré P, Daube O. Natural convection in a differentially heated horizontal cylinder: Effects of Prandtl number on flow structure and instability. *Physics of Fluids* 1997; **9**: 1014–1033.

5. Bergeon A, Henry D, BenHadid H, Tuckerman LS. Marangoni convection in binary mixtures with Soret effect. *Journal of Fluid Mechanics* 1998; **375**: 143–177.
6. Chenier E. Etude de la stabilité linéaire des écoulements thermocapillaires et thermogravitationnels en croissance cristalline. Thesis, Université Paris XI, LIMSI report 97-26, 1997.
7. Vanka SP. Block-implicit multigrid solution of Navier–Stokes equations in primitive variables. *Journal of Computational Physics* 1986; **65**: 138–158.
8. Trefethen LN. Pseudo-spectra of linear operators. *SIAM Review* 1997; **39**: 383–406.
9. Yu Gelfgat A, Tanasawa I. Numerical analysis of oscillatory instability of buoyancy convection with the Galerkin spectral method. *Numerical Heat Transfer A* 1994; **25**: 627–648.
10. Lehoucq RB, Sorensen DC, Yang C. *ARPACK Users Guide*. SIAM: Philadelphia, PA, 1998.
11. Hill DC. Adjoint systems and their role in the receptivity problem for boundary layers. *Journal of Fluid Mechanics* 1995; **292**: 183–204.
12. Le Quéré P , Transition to unsteadiness routes to chaos and simulation of turbulent flows in cavities heated from the side: a review of present status. In *Heat Transfer: Proceedings of the 10th International Heat Transfer Conference*, Hewitt GF (ed.). IchemE: Brighton, UK, vol. 1, 1994; 281–296.
13. Vanel JM, Peyret R, Bontoux P. A pseudo-spectral solution of vorticity–stream-function equations using the influence matrix technique. In *Numerical and Mechanical Fluid Dynamics*, vol. II, Morton KW, Baines MJ (eds). Clarendon Press: Oxford, 1986; 463–475.
14. Goda K. A multistep technique with implicit difference schemes for calculating two- or three-dimensional cavity flows. *Journal of Computational Physics* 1979; **30**: 76–95.
15. Saad Y, Schultz MH. GMRES: a generalized minimal residual algorithm for solving nonsymetric linear systems. *SIAM Journal of Scientific and Statistical Computing* 1986; **7**: 856–869.
16. Kleiser L, Schumann U. Treatment of incompressibility and boundary conditions in 3-D numerical spectral simulations of plane channel flows. Notes. In *Numerical Fluid Mechanics*, vol. 2, Hirschel EH (ed.). Vieweg: Wiesbaden, 1980; 165–173.
17. Le Quéré P, Alziary de Roquefort T. Computation of natural convection in 2-D cavities with Chebyshev polynomials. *Journal of Computational Physics* 1985; **57**: 210–228.
18. Tuckerman LS. Divergence free velocity field in non-periodic geometries. *Journal of Computational Physics* 1989; **80**: 403–441.
19. Daube O. Resolution of the 2D Navier–Stokes equations in velocity-vorticity form by means of an influence matrix technique. *Journal of Computational Physics* 1992; **103**: 402–414.
20. Gill AE. The boundary layer regime for convection in a rectangular cavity. *Journal of Fluid Mechanics* 1969; **26**: 515–536.
21. Bejan A. *Convection Heat Transfer*. Wiley: New York, 1984.
22. Gadoin E, Le Quéré P. Characterisation of unstable modes in partitioned cavities. In *Heat Transfer 1998: Proceedings of the 11th International Heat Transfer Conference*, Lee JS (ed.). Korean Society of Mechanical Engineers: Kyongiu, Korea, vol. 3, 1998; 429–434.
23. *Christodoulou KN*, *Scriven LE*. *Finding leading modes of a viscous free surface flow*: *an asymmetric generalized eigenproblem*. *Journal of Scientific Computing* 1988; **3**: 355–406.
24. Barkley D, Tuckerman LS. Stokes preconditioning for the inverse power method. In *Lecture Notes in Physics: Proceedings of the Fifteenth International Conference on Numerical Methods in Fluid Dynamics*, Kutler P, Flores J, Chattot J-J (eds). Springer: New York, 1997; 75–76.
25. Tuckerman LS, Bertagnolio F, Daube O, Le Quéré P, Barkley D. Stokes preconditioning for the inverse Arnoldi method. In *Notes on Numerical Fluid Mechanics*, vol. 74, Henry D, Bergeon A (eds). Vieweg: Wiesbaden, 2000; 241–255.
26. Sorensen DC. Implicit application of polynomial filters in a k-step Arnoldi method. *SIAM J Matrix Analysis Applications* 1992; **13**: 357–385.
27. Lehoucq RB. *Analysis and implementation of an implicitely restarted Arnoldi iteration*. PhD thesis, Rice University, 1995.
28. Winters KH. Hopf bifurcation in the double-glazing problem with conducting boundaries. *Journal of Heat Transfer* 1988; **109**: 894–898.
29. Tritton DJ. *Physical Fluid Dynamics*. Clarendon Press: Oxford, 1988.
30. Luchini P, Bottaro A. Görtler vortices: a backward-in-time approach to the receptivity problem. *Journal of Fluid Mechanics* 1998; **363**: 1–23.
31. Allan BG. A reduced order model of the linearized incompressible Navier–Stokes equations for the sensor/actuator placement problem. ICASE Report No. 2000-19, 2000.
32. Park HM, Lee MW. Control of Navier–Stokes equations by means of mode reduction. *International Journal Numerical Methods in Fluids* 2000; **33**: 535–557.
33. Giles MB, Pierce NA, An introduction to the adjoint approach in design. *Flow Turbulence and Combustion* 2000; **65**(3).
34. Hackbusch W. *Multigrid Methods and Applications*. Springer: Berlin, 1985.
35. Wesseling P. *An Introduction to Multigrid Methods*. Wiley: Chichester, 1992.

